

# FLOW AND HEAT TRANSFER CHARACTERISTICS OF HIGH-PRESSURE NATURAL GAS IN THE AIR GAP OF HIGH-SPEED MOTOR

*Qiang ZHAO<sup>1,2</sup>, Yichao YUAN<sup>1\*</sup>*

<sup>\*1</sup>School of Energy and Power Engineering, University of Shanghai for Science and Technology,  
Jungong Road 516, 200093 Shanghai, China

<sup>2</sup>Wolong Electric Nanyang Explosion Protection Group Co., LTD, Dushan Road 1801, 473000,  
Nanyang, China

<sup>\*</sup> Corresponding author; E-mail: yuanyichao@usst.edu.cn

*High-speed motors are widely used in industrial applications owing to their unique features, such as compact framework, high performance, and high reliability. Based on the finite volume method and numerical heat transfer theory, this study establishes a stator-air gap-rotor model, and the flow and heat transfer in the air gap between the stator and rotor in a high-speed motor are investigated with high-pressure natural gas as the cooling medium. Meanwhile, the “radial tri-vortex partition, alternating axial distribution” feature of the turbulent Taylor-Couette vortex in the air gap of the motor is determined. Then, the optimal structural parameters which can realize the heat transfer enhancement of motor air gap are obtained. Finally, an optical fiber grating temperature measurement system based on the wavelength division multiplexing technology is utilized to attain the temperature distributions on the stator and rotor surfaces. The simulation results are compared with the experimental data to evaluate the simulation method’s precision.*

*Key words: high-pressure natural gas, Turbulent Taylor vortex flow, high-speed motor, heat transfer enhancement*

## 1. Introduction

Owing to their compact structure, high efficiency, large power density, excellent integrability, and good reliability, high-speed motors are widely applied in equipment such as high-speed spindles, flywheel energy-storage systems, air-cooling cycle systems and high-speed natural gas centrifugal compressor, etc. [1-3]. To ensure sufficient strength of the motor rotor in high-speed operation, solid rotors are usually used. However, solid rotor is subjected to large vortex loss, and the surface of high-speed rotating rotor can produce large wind friction losses, which causes heating problem. Additionally, high-frequency current and high-frequency magnetic density of high-speed motors lead to severe heating of the motor [4-6]. The integrated compressor unit equipped with high-speed inductive motor uses high-pressure natural gas medium for direct cooling without needing any fan-powered components and cooling systems. Under high pressure, the thermal properties of natural gas cooling medium are quite different from the conventional cooling media (air or water). The natural gas inside the motor is extremely susceptible to generate the Taylor vortices due to the high Taylor number, and the flow state is more complex. Thus, it is necessary to investigate the Taylor vortex flow and heat transfer characteristics of high-pressure natural gas in the air gap.

The Taylor vortex flow state of conventional cooling mediums such as water and air and heat transfer characteristics has been extensively investigated through numerical simulation and experiments. David Andereck *et al.* [7] studied the flow state of water between concentric rotating cylinder, and proved that different flow states of the fluid (Taylor vortices, wave vortices, modulated wave vortices, vortices with wave outflow boundaries, vortices with wave inflow boundaries, etc.) are related to the Reynolds number of the fluid between the inner and outer cylinders. Coles *et al.* [8] conducted a detailed study for the helical turbulent zone present in the Couette flow between concentric rotating cylinders, determined the effect by interfaces and intermittency in the turbulent transition process. Burkhalter *et al.* [9] experimentally studied the supercritical Taylor vortex of fluids between cylinders with different ratios of length to diameter, and confirms that the wavelength of the Taylor vortex measured in a finite cylinder differs from the wavelength theoretically measured for an infinite length cylinder. Fenstermacher *et al.* [10] used laser Doppler velocimetry to study the turbulence transition in a fluid contained between concentric cylinders with the inner cylinder rotating, and tested the number and type of dynamic states exhibited by the fluid before becoming a Taylor vortex. Wereley *et al.* [11] used a particle image velocimetry (PIV) to measure the axial and radial velocities of non-wave and wave Taylor-Cuet flows in the annular space between the rotating inner cylinder and the fixed outer cylinder. The experimental results showed that the vortices become stronger as the Reynolds number increases and the outflow between pairs of vortices becomes increasingly jet-like. Additionally, the Taylor vortex flow state and cooling effect of the conventional cooling medium in the rotating machinery have been investigated by numerical simulation and experimental measurement [12-14].

Based on the optimization of the high-speed motor structure, there are very few reports on the Taylor vortex flow and heat transfer features of the cooling medium of high-pressure natural gas in the air gap, especially enhancing heat transfer through the slotting of the motor stator. In this paper, based on the finite volume method and numerical heat transfer theory, a stator-air gap-rotor geometric model is established, where the coupling mechanism of the stator and rotor heat source of high-speed motor, thermophysical properties of high-pressure natural gas, and geometric characteristics of air gap structure are comprehensively considered. The variation law of the internal flow and heat transfer characteristic of the air gap in the motor under a high-pressure natural gas cooling medium is revealed. Then, the relationship between the distribution of Taylor-vortex in air gap and the aspect ratio of the stator notch are studied in detail, and it is concluded that the aspect ratio of the stator notch affects the axial and radial velocity distribution of the cooling medium in air gap, By comparing the average heat transfer coefficient and average Nusselt number of the stator and rotor surfaces under the four aspect ratios of the stator slot, the optimized aspect ratio of the stator notch is determined. Finally, a high-speed motor flow and heat transfer experimental platform is established, and the temperature distributions inner the stator and rotor surfaces in the air gap are obtained by the fiber grating temperature measurement system. The accuracy of the research is demonstrated by comparing the numerical simulation with the experimental results.

## **2. Numerical model**

### **2.1. Physical model and boundary conditions**

A schematic of the compressor unit and the motor ventilation cooling system is presented in Fig.

1. To make the cooling system of the compressor unit more compact, the high-pressure natural gas is directly used to cool the high-speed motor without fan-powered components and additional cooler system, thereby constructing an inner circulation cooling system, where the cooling medium adopts the first-level outlet airflow of the compressor and flows back to the compressor inlet for re-compressing after the motor is cooled. The key to heat dissipation lies in the air gap structure feature. The number of stator slots is 42. Considering the symmetry of the high-speed motor model, 1/42 of the motor is taken as the research object during the numerical simulation of the motor air gap.

The motor parameters are listed in Tab. 1. The parameters without the physical dimension are used to describe the geometric characteristics of the motor. The radius ratio  $\eta = r_1 / r_2 = 0.97$ , the radial position is  $R^* = (r - r_1) / d$ , where the  $r$  is the radius of any point in the air gap, and the axial position is  $Z^* = z / d$ , whose value range is 0-50, where  $z$  is the distance between any point in the air gap and the entrance, the aspect ratio  $\Upsilon = a / b$ .

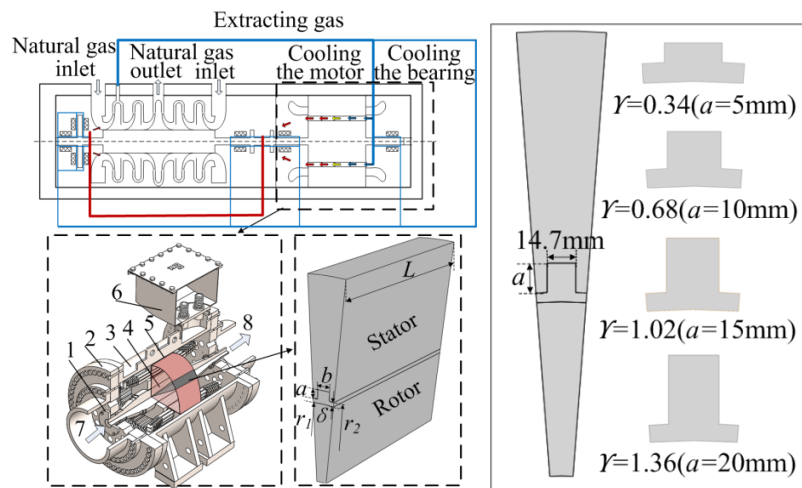


**Figure 1. Schematic of ventilation cooling system of integrated compressor and motor (1-bearing; 2-end cover; 3-frame; 4-rotor; 5-stator; 6-junction box; 7-inlet; 8-outlet)**

**Table 1. Main motor parameters**

Parameter	Value	Parameter	Value
Rated power/kW	160	Outer diameter of the stator/ mm	620
Rated voltage/kV	10	Inner diameter of the stator $r_2$ / mm	350
Rated frequency/Hz	100	Outer diameter of the rotor $r_1$ / mm	340
Number of stator slots	42	Length of core $L$ / mm	250
Number of rotor slots	32	Thickness of air gap $\delta$ / mm	5
Notch width $b$ / mm	14.7	Notch height $a$ / mm	5、10、15、20
Heat source of the stator/kW	2.25	Heat source of the rotor/kW	6.01

The commercial software Fluent 2020R1 is used for numerical simulation. The stator and rotor of the motor are set to a constant body heat source as shown in Tab. 1. The cooling medium in the air gap is 7MPa compressed natural gas. The velocity-inlet boundary condition is chosen at the inlet, and the inlet velocity is 0.406 m/s, the inlet temperature is 323 K. The pressure-outlet boundary condition is chosen at the outlet. The outer surface of the rotor is set as a rotating wall, and the rated rotation speed is 6000 rpm. The inner surface of the stator is set as the static coupling wall, and the other walls are set as the static adiabatic wall.

## 2.2. Calculation methods and grid independence test

The internal flow of the motor is in a turbulent state. The steady-state control relations for flow and heat transfer are used, including mass, momentum, and energy conservation equations. The shear-stress transport (SST)  $\kappa$ - $\omega$  model established by Menter is used as the turbulence model, which can accurately obtain the flow intensity and turbulent kinetic energy in the flow field, and thus the Taylor vortex and turbulent Taylor vortex transition process of the fluid can be obtained [15]. The pressure-velocity coupling equations are solved by coupled algorithm, the discrete format of convection terms use the second-order upwind scheme, the residual of the flow field is  $1 \times 10^{-6}$  and the residual of the temperature field is  $1 \times 10^{-8}$ .

In this paper, the models with  $\gamma = 0.34, 0.68, 1.02$ , and  $1.36$  are numerically simulated (Fig. 1). During the mesh division, the boundary layer grids of the inner and outer walls of the four models are same. The boundary layer mesh  $Y^+$  is less than 1, and the growth rate is 1.2. Figure 2 shows a schematic of the griding strategy and the air gap grid distribution with  $\gamma = 0.68$ .

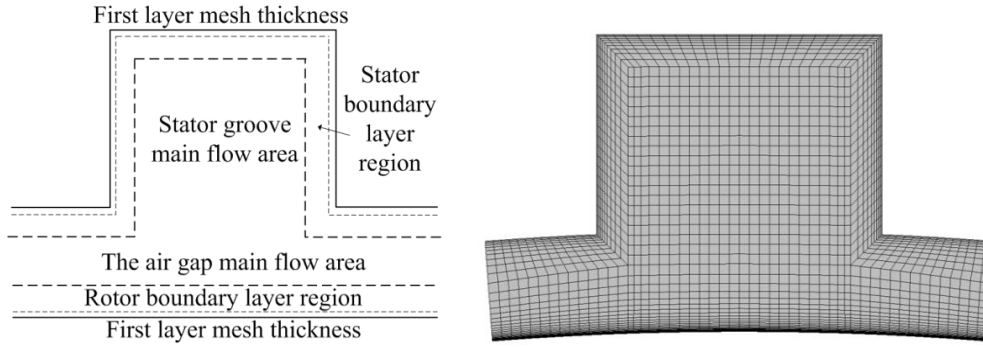


**Figure 2. Schematic of griding strategy and the air gap grid distribution with  $\gamma = 0.68$ .**

Figure 3 shows the results of grid independence test, four grid systems of 0.154 million, 0.199 million, 0.255 million and 0.312 million are studied. The difference of  $Nu$  number between the 0.154 million, 0.199 million, 0.255 million grids and 0.312 million grids is 19.8%, 10.3%, 3.1%, respectively. Therefore, the grid system of 0.255 million not only meets the requirements of calculation accuracy, but also saves computing resources. The grid system of 0.255 million is selected for subsequent research.

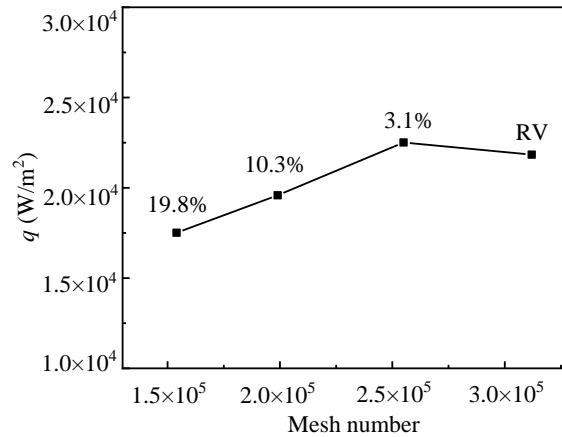


**Figure 3. Mesh independence test at  $a=10m$ ,  $Re=9890$ ,  $Ta=4.8E+10$**

### 2.3. Numerical method validation

In order to verify the correctness of the numerical calculation method used in this paper, the numerical calculation results of the smooth air gap structure are compared with the Tachibana equation [20], which is shown in Eq. (1). Figure 4 shows the axial distribution of  $Nu$  number on the surface of the air gap rotor with five different  $Ta$  numbers. Table 2 shows the comparison between the numerical mean value and the calculated value of Tachibana equation. The maximum deviation of  $Nu$  number is 7.5%. The numerical simulation results are in good agreement with the empirical formula, which can ensure the accuracy of the numerical simulation results.

Tachibana equation:

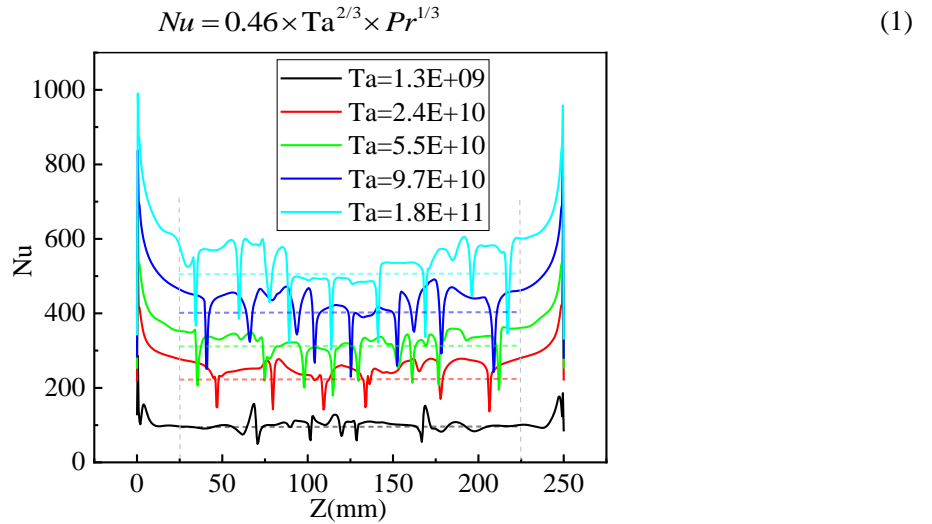


Figure 4. Axial distribution of  $Nu$  number on the surface of air gap rotors with five  $Ta$  numbers

Table 2. Comparison between numerical calculation results and empirical formulas

Case	$Ta$	Numerical mean value	Tachibana equation value	Deviation
1	1.26E+09	99.8	95.2	4.9%
2	2.43E+10	250.8	255.1	-1.7%
3	5.47E+10	321.1	334.2	-3.9%
4	9.73E+10	426.3	404.9	5.3%
5	1.77E+11	531.9	494.5	7.5%

## 3. Results and discussion

### 3.1. Distribution characteristics of turbulent Taylor vortex

In order to study the influence of stator slot on the distribution characteristics of turbulent Taylor vortex in the motor air gap, Figure 5 shows the meridian vorticity cloud map and local velocity vector diagram of air gap in the motor with  $\gamma = 0.68$ , where the axis  $Z^*=15-22$  is selected. This area contains two pairs of Taylor vortex, reflecting the flow characteristics in the motor air gap.

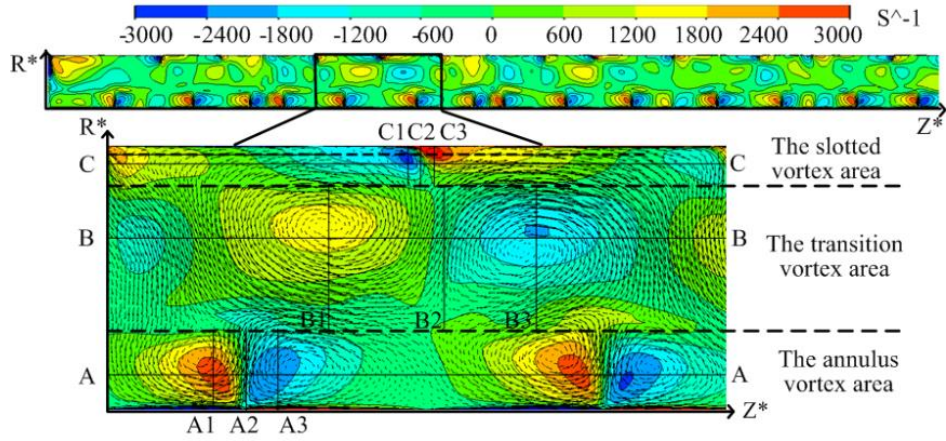


**Figure 5. Meridian vorticity cloud diagram and local velocity vector diagram of air gap in the motor ( $\gamma=0.68$ )**

It is clear from Fig. 5 that the flow field in the motor's air gap is in a turbulent Taylor-Couette flow state. The airflow starts to form Taylor vortex pairs after a certain distance from the inlet of the air gap due to the inlet effect. According to the distribution characteristics of the vorticity and velocity vector in the figure, the air gap flow can be categorized into three regions:

The area  $R^*=0-1$  around the rotor surface is defined as the annulus vortex area, and its Taylor vortex is called the annulus large-scale vortex cell. The centre line A-A of the vortex cell is located near  $R^*=0.5$ , and the vorticity remains the same. The vortex cell is wide at the top and narrow at the bottom, arranged oppositely on the left and right.

The area  $R^*=2.5-3$  near the stator slot's inner surface is defined as the slotted vortex area, and its Taylor vortex is called the slotted small-scale vortex cell. The centre line C-C of the vortex cell is located near the wall surface at  $R^*=2.9$ , and the vortex cell is narrow at the top and wide at the bottom, alternately arranged on the left and right.

The intermediate area  $R^*=1-2.5$  between the annular vortex area and the slotted vortex area is defined as the transition vortex area. The inner Taylor vortex is called the transitional energy dissipating vortex cell. The vortex centre line B-B is located in the middle of the stator slot at  $R^*=2$ , and the vortex is relatively small. The vortex cell is elliptical in the axial direction and arranged separately on the left and right.

Based on the above analysis, the turbulent Taylor-Couette vortex distribution characteristics of "radial three-vortex partitions, alternating axial distribution" in the air gap of high-pressure natural gas cooling motor are determined, which promotes the transportation of the natural gas medium along the axial and the radial direction.

### 3.2. Velocity and temperature distribution in the air gap

To study the influence of Taylor vortex on the flow and heat transfer in air gap under the slotted model with  $\gamma=0.68$ , the velocity, temperature, and density in the radial and axial orientations are systematically investigated, and the influence mechanism of Taylor vortex on the flow and heat transfer characteristics in the motor air gap is examined. Further, the influence law of Taylor vortex on the air gap fluids' heat transfer characteristics in the slotted model is revealed.

#### (1) Velocity and temperature distribution along the axial direction in the air gap

According to Fig. 6, the radial and axial velocities of the three vortices within the air gap change periodically.

The radial velocity at the centre line A-A of the annulus Taylor vortex cell shows a hump-shaped distribution along the axial direction with a large amplitude, and the axial velocity fluctuates along the axial direction with the smallest amplitude. The temperature fluctuation of the cooling medium increases along the axial orientation, and the temperature near the middle of the vortex pair has an obvious sudden change.

The radial and axial velocities at the centre line B-B of the Taylor vortex cell in the transition zone show a cosine-like distribution along the axial direction. The radial velocity has the largest amplitude, and the amplitude of axial velocity is relatively small. There is a sharp increase in the position between two adjacent pairs of Taylor vortex.

The radial velocity at the centre line C-C of the slotted Taylor vortex shows a shallow V-shaped distribution along the axial direction with the smallest amplitude, while the axial velocity oscillates periodically with a wave shape along the axial direction with a larger amplitude.

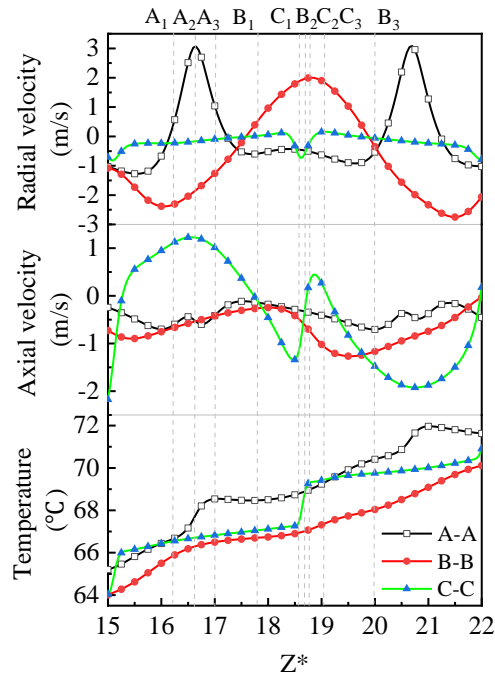


**Figure 6. Axial distribution of the velocity and temperature along the vortex cell's centre line in the three radial zones**

The temperature of the high-pressure natural gas cooling medium increases continuously along the axial direction at the centre line position of the three radial vortices, and it basically presents a trend with high temperature on both sides and low temperature in the middle along the radial direction, i.e.,  $TA-A > TC-C > TB-B$ , indicating that the heat of the stator and rotor is exchanged with the cooling medium through the wall, and then it is transferred to the transition zone to remove the heat.

There is a sharp increase in temperature at the centre positions A2 and B2 of the vortex cell in the annulus and slot, and the temperature rises sharply at the centre of the A1-A3 and C1-C3 vortex pairs. This is because the radial velocity at the position of the annulus vortex cell along the axial direction changes significantly. The radial velocity at the centre of the vortex cell reaches the maximum value of 3.08 m/s, which brings the heat of the rotor to the transition zone. The radial and



axial velocities of the slotted vortex cell change sharply, which brings the heat of the stator to the transition zone.

## (2) Velocity and temperature distribution along the radial direction in the air gap

Figure 7(a) depicts the axial velocity distribution curve of the radial three-zone vortex cells. The absolute value of the axial velocity at the centre line of three-zone vortex cell pairs is the smallest, and it fluctuates around 0 m/s. The axial velocity at the junction of three zones changes greatly. In particular, the absolute value of the axial velocity at the junction of the transition zone and the adjacent zone is maximum, which is conducive to the heat dissipation.

Figure 7(b) describes the radial velocity distribution curve of the radial three-zone vortex cell. The absolute value of the radial velocity at the centre line of the three-zone vortex cell pairs is the largest, and the maximum value of the annulus vortex is 3.06 m/s, indicating that the convective heat transfer is fastest in the middle of vortex cell pairs. Further, the radial velocity of the vortex cell pair in the annular gap causes flow from the stator inner surface to the transition zone, which is beneficial to eliminate the heat from the stator. The transition zone is farther apart, and the radial velocity at the centre line of the vortex cell pair is larger, where the flow is from the rotor to the stator side. The velocity at the centre line in the two vortex cells is smaller, and the flow is from the stator side to the rotor side, which is conducive to the heat exchange process.

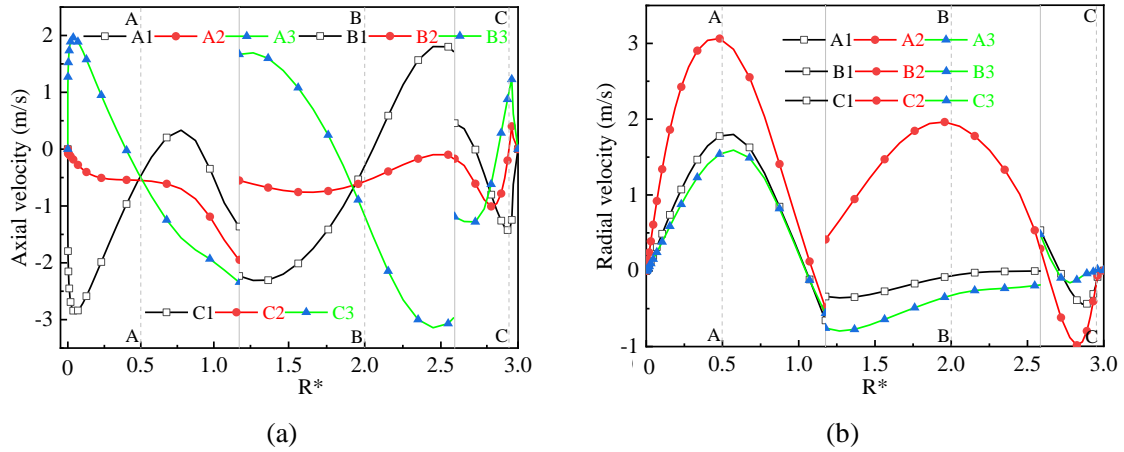


Figure 7. Axial velocity: (a) radial velocity; (b) distribution of vortex cell pairs

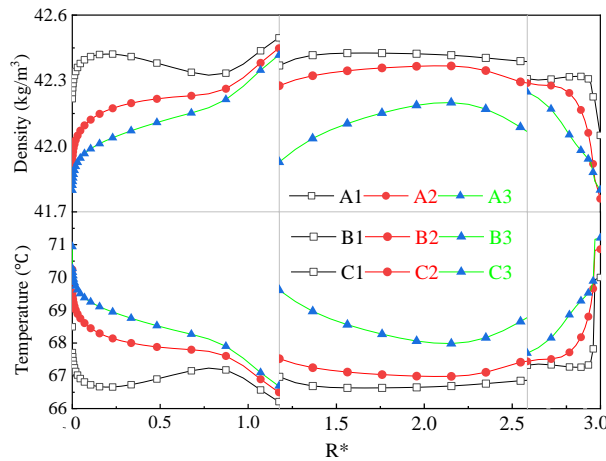


Figure 8. Density and temperature distribution of the vortex cell pair



Due to the interactive change of the axial and radial velocities in the vortex cell, the radial temperature of the vortex cell is changed. The temperature in the annulus gap and the slot area changes more drastically. Meanwhile, the radial density in the vortex cell changes symmetrically due to the change in temperature. Figure 8 presents the density and temperature distribution curve at the radial centre line of the vortex cell pairs. The variation trend of the density in different vortex regions is opposite to the temperature change trend, and the change in the density of cooling medium aggravates the velocity change in the vortex cell, which indirectly affects the temperature.

### 3.3. Heat transfer characteristic between the stator and rotor

Figure 9 shows the heat flux distribution and a partially enlarged perspective of the surface of the rotor ( $Z^*=15-22$ ). The heat flux has periodic fluctuations similar to the change in radial velocity. This shows that the existence of turbulent Taylor vortex considerably influences the heat transfer process, and it increases the axial and radial flow of the cooling medium, so there is an intense heat exchange between the rotor surface and the cooling medium.

To further examine the impact of the Taylor vortex on the wall heat flux density distribution, the heat flux density at linear positions of  $x = 0$  and  $Z^* = 18.5$  in Fig. 9 are extracted. And the influence of the Taylor vortex on the wall heat flux density distribution in the axial and circumferential orientations is studied. The heat flux density on the rotor surface at  $x = 0$  alternately fluctuates along the axial orientation, consistent with the axial turbulent Taylor-Couette vortex distribution in the annulus vortex (shown in Fig. 5). The heat flux density difference between the centre and the adjacent Taylor vortex pair is relatively large, decreasing from  $27788 \text{ W/m}^2$  to  $16180 \text{ W/m}^2$ , and the percentage change is 41.8%. This change is drastic, and while the heat flux density in the other positions is uniform. The maximum value of the heat flux density on the rotor surface at  $Z^*=18.5$  is  $23570 \text{ W/m}^2$ . A small wave crest appears between the two large wave crests, and the maximum value of the small wave crest is about  $23000 \text{ W/m}^2$ . The heat transfer effect is relatively enhanced, revealing that the slotted structure of the stator enhances the circumferential flow and heat transfer on the rotor surface, which is beneficial to improve the rotor surface's heat transfer capacity.

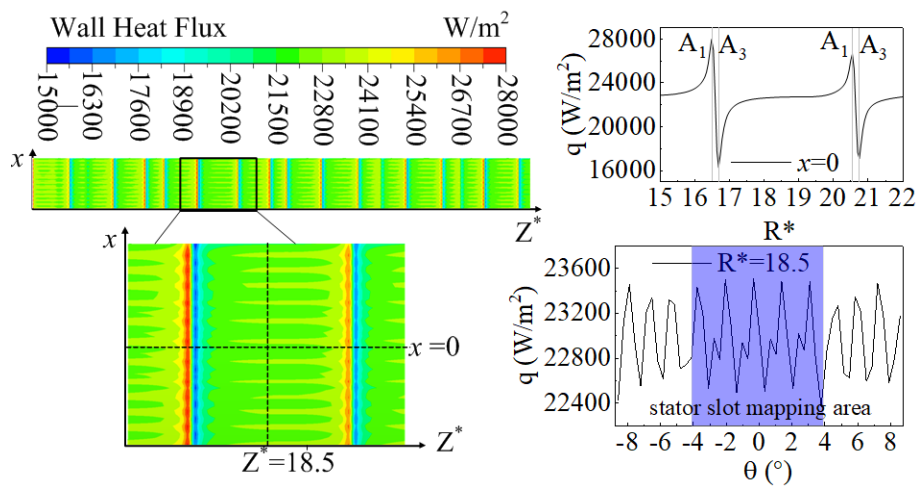
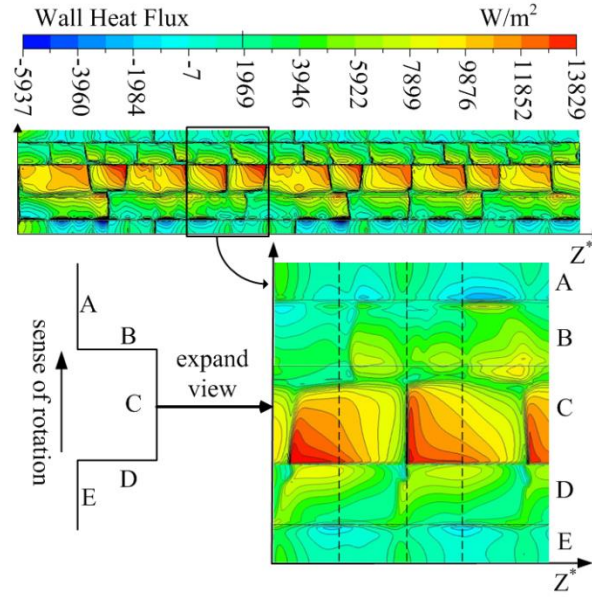


Figure 9. Heat flux density distribution of the rotor surface

Different from the rotor's wall heat flux density distribution, the stator surface has local heat flux concentrated in a corner of the slot. Figure 10 presents the heat flux distribution and a partially

enlarged view of the stator surface ( $Z^*=15-22$ ). The heat flux density on the stator surface alternately fluctuates along the axial orientation, where the heat flux density on the stator surface C is the largest, and its maximum value is  $13829 \text{ W/m}^2$ . The heat flux densities on surfaces B and C of the stator are in the middle, while the heat flux density on surfaces A and E of the stator is the smallest, and its minimum value is  $-5937 \text{ W/m}^2$ , resulting in the heat absorption phenomenon.



**Figure 10. Heat flux density distribution of the stator surface**

The heat flux density on the C surface of the stator alternately fluctuates along the axial direction, which is consistent with the axial turbulent Taylor-Couette vortex distribution in the slotted vortex area (Fig. 5). The difference in the heat flux between the centre of the Taylor vortex pair and the adjacent Taylor vortex pair is large. The heat flux density in other positions changes uniformly, indicating that the presence of turbulent Taylor vortex strengthens heat transfer at the C surface and enhances the convective heat transfer of the stator.

Under the effects of the circumferential and axial velocities, the airflow enters the slotted area of stator along the wall of the slot facing the rotation direction of the rotor, and the inner surface of the stator is subjected to the wall impact and vortex effect, which strengthens the heat exchange capacity between the cooling medium and the wall. Due to the effect of circumferential speed of the motor, the surfaces D and E of the stator surface exhibit local negative pressure under the impact of the wall surface B and the separation effect of the surface C, which is not conducive to heat dissipation of stator.

### 3.4. Influence of on the aspect ratio of the stator notch on the heat transfer in the air gap

The average heat transfer coefficient and average Nusselt number on the rotor surface are presented in Fig. 11(a). The average Nusselt number gradually increases as the aspect ratio of the stator notch increases, and the maximum value is 2464. The convective heat transfer coefficient first grows and then declines while increasing the aspect ratio. The heat transfer coefficient is maximum ( $6526 \text{ W/m}^2\text{K}$ ) at  $\gamma = 0.68$ , which is 8.98% higher than that at  $\gamma = 1.36$ .

The average heat transfer coefficient and average Nusselt number on the stator surface are shown in Fig. 11(b). The average Nusselt number initially increases and then decreases as the aspect

ratio of the stator slot increases, and it reaches the maximum value of 908 at  $\gamma = 1.02$ . The average heat transfer coefficient first grows and then declines while increasing the aspect ratio, and it is maximum (2656 W/m<sup>2</sup>K) at  $\gamma = 0.68$ , which is 21.2% higher than that at  $\gamma = 1.36$ .

The comprehensive analysis of the average heat transfer coefficient on the stator and rotor surfaces suggests that it is the largest at  $\gamma = 0.68$ , while the Nusselt number exhibits a slight increase and decrease with the increase in the aspect ratio, and the change is not large. Therefore, the optimal aspect ratio of the stator notch is  $\gamma = 0.68$ .

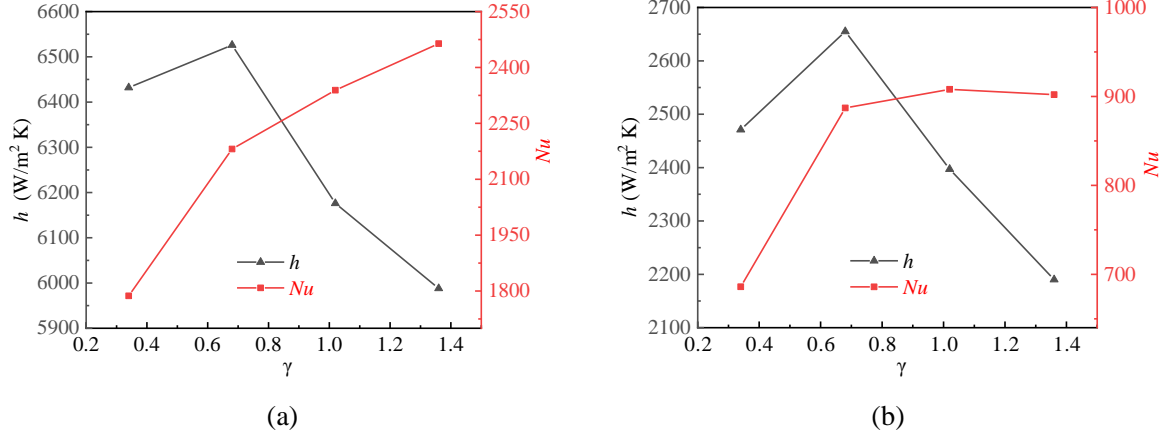


**Figure 11. Average heat transfer coefficient and average Nusselt number: (a) the rotor surface; (b) the stator surface**

#### 4. Test and verification

This experiment platform for the study of internal flow and heat transfer characteristics comprises four components: a constant-temperature and constant-pressure air source system, a high-speed inductive asynchronous motor, motor temperature test system, and a fiber grating temperature measurement system, as shown in Fig. 12. Constant-temperature and constant-pressure gas supply system provides a constant temperature, flow and pressure cooling gas source for the motor. The high-speed induction asynchronous motor is with  $\gamma = 0.68$ . The losses of the various parts of the motor operating at rated condition can be tested. The optical fibre grating pyrometer is based on the principle of optical fibre grating sensor, using the wavelength division multiplexing method. The sensor connection could be serial, parallel and in ring connection, and the motor rotor temperature can be tested dynamically[16-19]. The motor's temperature rise was tested at the motor test centre of Wolong Electric Nanyang Explosion-proof Group Co., Ltd. The field test system is shown in Fig. 12.

Figure 13(a) plots the distribution position of the grating fiber temperature sensor in the air gap of the test section. There are 19 temperature measuring points distributed in the air gap of the motor. The centre position A of stator slot and the centre position B of air gap are arranged with 2 sensors in the inlet and outlet along the axial direction. The stator inner surfaces C and D are arranged with 10 sensors along the axial direction, and the rotor surface E is arranged with 5 sensors along the axial direction. The temperature sensor on the rotor surface is connected to the fiber grating demodulator through a fiber optic rotary connector for data recording.

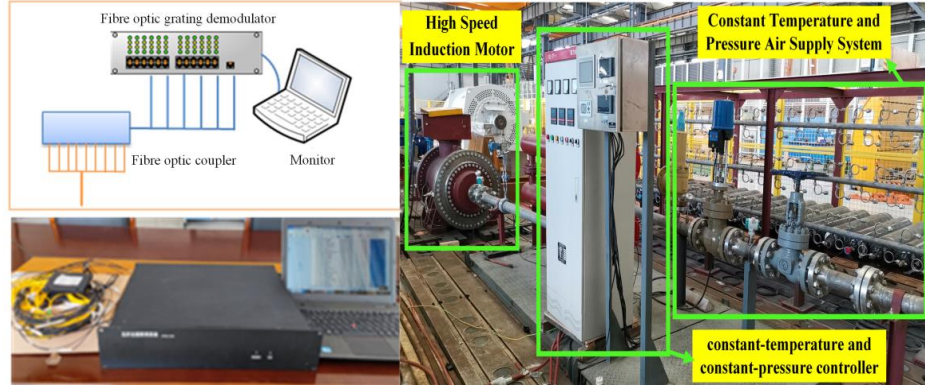


Figure 12. Test system

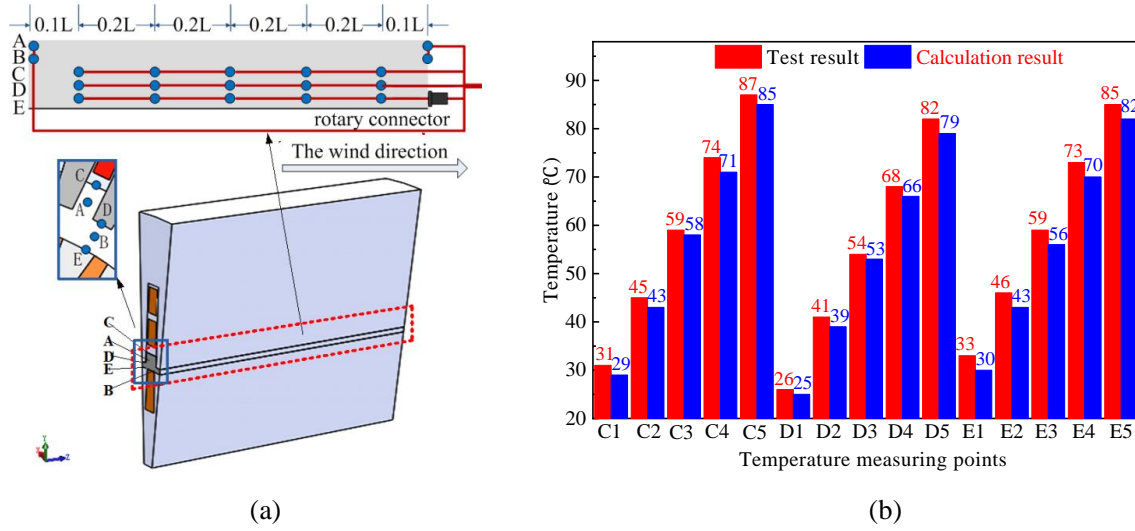


Figure 13. Temperature measuring points in the motor air gap: (a) the position of the grating fiber temperature sensor; (b) the results

The results of the tested and numerical calculation values of the motor are shown in Fig. 13(b). By comparing the numerical calculation results of the motor temperatures with the experimental data, it can be found that the experimental and numerical calculation temperatures of the motor both gradually increase with the axial length variation, and the growth trend of temperatures is consistent. At the temperature measuring points C1-C5, the maximum temperature difference between the examined and numerical calculation values is 3°C, the maximum error is 7.7%. At the temperature measuring points D1-D5, the maximum temperature difference between the examined and numerical calculation values is 2°C, the maximum error is only 5.7%. At the temperature measuring points E1-E4, the temperature maximum error between the examined and numerical calculation values is on E1, the maximum error is 8.6%. It proves that the numerical simulation method used in this paper is accurate.

## 5. Conclusion

To study the flow and heat transfer characteristics in the air gap of the high-speed motor with the cooling medium of high-pressure natural gas, a stator-air gap-rotor geometric model is established in which the coupling mechanism of the stator and rotor heat source of high-speed motor, thermophysical properties of high-pressure natural gas, and geometric characteristics of air gap

●Based on the characteristic of the annulus gap-slot flow partition, and the turbulent Taylor-Couette vortex distribution characteristics of "radial three-vortex partitions, alternating axial distributions" in the air gap under high-pressure natural gas cooling motor are determined. Specifically, a three-zone vortex diagram composed of annulus vortex, transition vortex, and slotted vortex is established. The radial and axial velocities along the axial direction of centre lines of three radial vortices in the air gap show periodic changes.

●A non-linear relationship is determined between the heat transfer in the motor's air gap and the aspect ratio, and the optimized structural parameters are obtained to achieve enhanced heat transfer under the axial cooling of high-pressure natural gas in the high-speed solid rotor. When the aspect ratio is 0.68, the stator and rotor surfaces' heat transfer coefficients reach the maximum values, which are 21.2% and 8.98% higher than those obtain at the aspect ratio of 1.36, respectively, indicating a relatively better heat transfer effect.

*a* –depth of the notch, [mm]  
*b* –width of the notch, [mm]  
*h* –heat transfer coefficient, [ $\text{Wm}^{-2}\text{k}^{-1}$ ]  
*L* –air gap length, [mm]  
*Nu* –Nusselt number ( $=hl/\lambda$ ), [–]  
*Pr* –Prandtl number ( $=\mu c_p/\lambda$ ), [–]  
*q* –heat flux, [ $\text{Wm}^{-2}$ ]  
*r* –radial lengths, [mm]  
*r<sub>1</sub>* –rotor outer diameters, [mm]  
*r<sub>2</sub>* –stator inner diameters, [mm]  
*Re* –Reynolds number ( $=UD/v$ ), [–]  
*R\** –nondimensional axial position  
( $R^*= (r - r_1)/\delta$ )  
*Ta* –Taylor number ( $= \rho^2 \omega^2 r D^3 / \mu^2$ ), [–]  
*x, y, z* – Cartesian coordinates  
Y+ – nondimensional first layer mesh thickness ( $= y \mu_\tau / \nu$ ), [–]  
*Z\** –nondimensional axial position  
( $Z^*= z/\delta$ )

### Greek symbols

$\delta$  –air gap thickness, [mm]  
 $\eta$  –nondimensional radius ratio ( $\eta = r_i/r_2$ )  
 $\gamma$  –nondimensional aspect ratio ( $\gamma = a/b$ )

- [1] Gerada, D., *et al.*, Design Aspects of High-Speed High-Power-Density Laminated-Rotor Induction Machines, *IEEE Transactions on Industrial Electronics*, 58 (2011), 9, pp. 4039-4047
- [2] Hong, D. K., *et al.*, Development of a High Speed Induction Motor for Spindle Systems, *IEEE Transactions on Magnetics*, 49 (2013), 7, pp. 4088-4091
- [3] Oguz, A. H., *et al.*, Design and Optimization of an Axially-Slitted High-Speed Solid Rotor Induction Motor, 2015 9th International conference on Electrical and Electronics Engineering

- (ELECO), Bursa, Turkey, 2015, pp. 568-573
- [4] Cao, J. W., Lei, Q., Design and Experiment of High Speed Motor Test System, CSAA/IET International Conference on Aircraft Utility Systems (AUS 2018), Guiyang, 2018, pp. 1139-1143
  - [5] Qi, Z. N., *et al.*, Thermal and Stress Analysis for a High-speed Permanent Magnet Motor with Solid Rotor, 2021 IEEE 4th Student Conference on Electric Machines and Systems(SCEMS), Huzhou, China, 2021, pp. 1-5
  - [6] Gao, Q. X., *et al.*, Copper Loss Analysis and Loss Separation Method in a Dynamic Process of Ultra-High Speed Motor with Slotless Stator, *IET Electric Power Applications*, 17 (2023), pp. 464-473
  - [7] David Andereck, C. *et al.*, Flow Regimes in a Circular Couette System with Independently Rotating Cylinders, *Journal of Applied Fluid Mechanics*, 164 (1986), pp. 155–183
  - [8] Coles, D., Transition in Circular Couette Flow, *Journal of Applied Fluid Mechanics*, 21 (1965), 3, pp. 385–425
  - [9] Burkhalter, J. E., Koschmieder, E. L., Steady Supercritical Taylor Vortex Flow, *Journal of Applied Fluid Mechanics*, 58 (1973), 3, pp. 547-560
  - [10] Fenstermacher, P., *et al.*, Dynamical Instabilities and the Transition to Chaotic Taylor Vortex Flow, *Journal of Applied Fluid Mechanics*, 94 (1979), 1, pp. 103-128
  - [11] Wereley, S.T, LUEPTOW R.M., Spatio-Temporal Character of Non-wavy and Wavy Taylor-Couette Flow, *Journal of Applied Fluid Mechanics*, 364 (1998), pp. 59-80
  - [12] Liang, X., *et al.*, Experimental and Numerical Investigation of Thermal Field for a Motor and Related Factors Sensitivities Using Combined CFD-Taguchi Method, *Thermal Science*, 23 (2019), 4, pp. 1065-1077
  - [13] Leng, S., Jin L. Q., Numerical Simulation of Heat Dissipation of Surface Mounted Permanent Magnet Synchronous Hub Motor, *Thermal Science*, 25 (2021), 6, pp. 4059-4066
  - [14] Jiade, H., *et al.*, Research on Taylor Vortex's Flow and Heat Transfer Characteristics of the Air Gap of the Motor (in Chinese), *Journal of Harbin University of Science and Technology*, 23 (2018), 2, pp. 114- 119
  - [15] Smirnov, P. E., Menter, F. R., Sensitization of the SST Turbulence Model to Rotation and Curvature by Applying the Spalart-Shur Correction Term, *Journal of Turbomachinery*, 131 (2009), 4, pp. 041010
  - [16] Mohammed, A., Djurović. S., A Study of Distributed Embedded Thermal Monitoring in Electric Coils Based on FBG Sensor Multiplexing, *Microprocessors Microsystems*, 62 (2018), pp. 102-109
  - [17] Mohammed, A., Djurović. S., Stator Winding Fault Thermal Signature Monitoring and Analysis by In Situ FBG Sensors, *IEEE Trans. Ind. Electron*, 66 (2019), 10, pp. 8082-8092
  - [18] Zhao, Q., *et al.*, Research on a High-Accuracy Dynamic Test Method of the Rotor Temperature Field of an Explosion-Proof Motor, *High Temperatures-High Pressures*, 49 (2020), 5, pp. 397-409
  - [19] Gunawardena, D. S., *et al.*, Regenerated Polymer Optical Fiber Bragg Gratings with Thermal Treatment for High Temperature Measurements, *Photonics Research*, 10 (2022), 4, pp. 1011-1021
  - [20] Tachibana, F., *et al.*, Convective Heat Transfer of the Rotational and Axial Flow between Two Concentric Cylinders, *Bulletin of JSME*, 7 (1964), 26, pp. 385-391

Submitted: 3.06.2023.  
Revised: 28.07.2023  
Accepted: 04.08.2023.